An Extensive Study of Shear Thinning Flow Around a Spherical Particle for Power-Law and Carreau Fluids

Carole-Anne Daunais[a], Lucka Barbeau[a], Bruno Blais[a,*]

[a] *Research Unit for Industrial Flows Processes (URPEI), Department of Chemical Engineering, Polytechique Montréal, PO Box 6079, Stn Centre-Ville, Montréal, QC, Canada H3C 3A7*

Abstract

We develop and implement a high-order finite element formulation to solve incompressible shear thinning flows using power-law and Carreau rheology models. We verify the implementation using the Method of Manufactured Solutions (MMS) and demonstrate that the implementation preserves the order of accuracy of the FEM scheme. We run high-order flow-past-a-sphere simulations for $\mathrm{Re} \in [0.1, 100]$ for Newtonian and shear thinning flows. Power-law simulations cover $n \in [0.3, 0.9]$, Carreau simulations cover the same range of n and dimensionless relaxation times $\Lambda \in [0.1, 100]$. We use 3D Cartesian grids, adopting a high-order sharp-interface immersed boundary method (IBM) to impose the no-slip boundary condition on the surface of the sphere. We use dynamic mesh adaptation with a Kelly error estimator to adaptively refine the grid. Newtonian drag coefficients are compared to Clift *et al.*'s model. Using the power-law model for shear thinning flow, results show that when decreasing n : the drag coefficient increases for $\mathrm{Re} \lessapprox 5$, it decreases for $\mathrm{Re} \gtrapprox 5$, and that for higher Reynolds the wake region is longer and the separation point is moved upstream. These drag coefficient results are in adequation with previously established simulation results. We provide a new drag coefficient correlation for power-law fluids that is valid for a wide range of n and for $\mathrm{Re} \in [0.1, 100]$, with $R^2 = 0.998$. The power-law model is singular in the zero-shear limit, and this limit is bound to occur in a flow-past-a-sphere geometry. For that matter, the Carreau model is well-posed. As the Carreau-modeled results show, the drag force on the sphere is considerably affected by the initial Newtonian plateau of the fluid. Drag coefficient results in the creeping flow regime are compared to experimental results, allowing validation of the numerical model. This work provides a better understanding of shear thinning flow past a sphere, for which the relationship between drag and flow regimes are highly nonlinear.

Keywords: Computational Fluid Dynamics, Power-Law, Carreau, Shear Thinning Flow, High-Order Methods, Drag Force on Sphere

*Corresponding author
Email address: bruno.blais@polymtl.ca (Bruno Blais)

1. Introduction

Understanding the behavior of diluted particle suspensions in shear thinning flows is fundamental to the chemical processing industry. While water is a Newtonian fluid, many water-based cosmetic, pharmaceutical, and agrifood products will experience shear thinning behaviors, meaning that their viscosity will decrease when shear is applied [1]. Molten plastics also play a massive part in the shear thinning fluid industry. Various unit operations treat shear thinning fluids using spherical particles such as packed and fluidized beds, or mechanical/chemical separation [2].

An effective way to understand the behavior of shear thinning flow through particle suspensions is to develop models that predict the flow pattern around the particles, and the forces that the fluid applies on them. To do so, it is appropriate first to study shear thinning flow past a single sphere.

The drag force on a single sphere in non-Newtonian fluids has been studied for over half a century. This section draws a brief overview of this study. On power-law modeled flow past a sphere [3], Adachi *et al.* (1973) studied the impact for $n \in [0.8, 1.0]$ at $\mathrm{Re} = 60$ as well as for creeping flow using a statistical method (method of moments) [4]. They concluded that the drag force increases when decreasing n notwithstanding the flow regime. They also determined that the wake region is longer for shear thinning flows. Acharya *et al.* (1976) are seemingly the first to experimentally study the case of a falling sphere in inelastic and elastic shear thinning fluids for $\mathrm{Re} \in [0.001, 1000]$ with $n \in [0.45, 1]$ [5]. They developed an expression for the drag coefficient as a function of n and Re. With a finite difference scheme, Lockyer *et al.* (1980) extended the n range to $[0.4, 1.0]$, without specifying the Reynolds number range [6]. To our best knowledge, they were the first to capture that the drag force on spheres in shear thinning flow increases for what they define as low Reynolds numbers and decreases for what they define as high Reynolds numbers when compared to Newtonian flow, which does not necessarily contradict the previous authors. They proposed an expression for the drag coefficient as a function of n for creeping flow. The article, however, omits to report a grid convergence analysis and a domain size analysis. Dahzi & Tanner (1985) introduced a finite element solver for power-law Stokes flow with $n \in [0.1, 1.0]$, and they also proposed an expression for the drag coefficient as a function of n [7]. Grid convergence results were not reported, but we assume the authors performed their simulations with due diligence. Still considering a creeping flow regime, Kawase & Moo-Young (1986) employed a perturbation approximation using an expression for the stream function to quantify the drag force for $n \in [0.6, 1.1]$, also concluding that the drag force increases as n decreases [8]. Tripathi *et al.* (1994) enlarged their flow regime range to $\mathrm{Re} \in [0.01, 100]$ with $n \in [0.4, 1.0]$ around spheroids, numerically solving using a finite element method [9]. They performed a domain size convergence analysis in conjunction with a mesh size analysis (using cylindrical

coordinates in 2D). However, the analyses results are not portrayed in the article, and the Re and n values used for these analyses are not specified. Tripathi *et al.* again observed that, as n decreases, the drag force is higher for low Re and lower for high Re, and they additionally found that this switch in the shear thinning effect happens between $\mathrm{Re} = 2$ and $\mathrm{Re} = 5$. They established that the wake length decreases for high Reynolds as n decreases, which thus contradicts Adachi *et al.* Renaud *et al.* (2004) gathered experimental drag coefficients from other authors for $\mathrm{Re} \in [0.1, 1000]$ and developed a correlation for C_D a function of Re and n for $n \in [0.2, 1.0]$. Their correlation for C_D has an average error of 21% for $\mathrm{Re} \leq 1$ and 16% for $\mathrm{Re} \geq 1$. This error is mainly attributable to viscoelastic and wall effects. They also acknowledge the switch in drag at $\mathrm{Re} = 5$ [10]. Dhole *et al.* (2006) adopted a finite volume method approach to simulate power-law modeled flow for $\mathrm{Re} \in [5, 500]$ and $n \in [0.5, 2.0]$ [11]. They performed a domain size analysis along with a grid size analysis. They observed that the drag force decreases in shear thinning fluids, which meets with Tripathi *et al.*'s conclusions. Like Adachi *et al.* predicted, they noticed that the wake is larger as n decreases. Song *et al.* (2009, 2011) simulated a falling sphere in power-law fluids for $\mathrm{Re} \in [1, 100]$ and $n \in [0.2, 1.0]$ using a FEM commercial software while comparing with experimental data [12, 13]. They performed a thorough study on the impact of the domain size, characterized by the ratio of the diameter of the sphere to the diameter of the cylindrical domain, on the simulation results. They must have carried out a mesh independence analysis but it is not shown in their work. They study the impact of n and of the domain size on the drag coefficient, the recirculation (wake) length and the separation angle. They provide an expression for C_D for a sphere over cylinder diameter ratio of over 0.21, that is out of scope of this present study. They also concluded that the wake region is larger as n decreases.

Regarding Carreau model studies, Chhabra & Uhlherr (1980) were seemingly the first to analytically derive an expression for the drag force considering a Carreau-modeled fluid for $n \in [0.2, 1.0]$ and dimensionless relaxation times $\Lambda \in [10^{-1}, 10^{3}]$ for creeping flow, that they experimentally validated [14]. They extended this study to intermediate flow regime (1980) for $n \in [0.52, 1]$, $\mathrm{Re} \in [0.032, 394]$ and dimensionless relaxation times $\Lambda \in [0.032, 630]$ [15]. They developed an expression of C_D with a maximal deviation of 14% when compared to experimental data they gathered. They concluded that the variation in the drag force is a function of n and Λ, but is independent of Re. Bush & Phan-Thien (1984) took Chhabra & Uhlherr's work and extended their research to $n \in [0.1, 1.0]$ using a boundary element method [16]. They concluded that the drag force increases in shear thinning creeping flow up until $n = 0.3$ and started to decrease after that. Bush & Phan-Thien conducted a grid convergence analysis only considering Newtonian creeping flow. Hsu *et al.* (2008) numerically studied the drag on a sphere in a particle suspension in Carreau fluids for $n \in [0.3, 1]$, for $\mathrm{Re} \in [0.1, 100]$ with $\Lambda \in [0, 10]$ [17]. They simulated the flow around a single sphere for an artificial void fraction $\epsilon \in [0.27, 0.999]$. They perform a domain size analysis, while the choice of mesh (FEM) is not discussed. They developed an expression for C_D for $\epsilon < 0.7$, which is highly ap-

propriate for the study of particle suspensions but slightly out of scope for this paper since we are interested in the flow around a single sphere. They concluded that the drag decreases when increasing Λ; this agrees with the observations of Chhabra & Uhlherr in the creeping flow regime.

What emerges from this overview is that most of the studies center on creeping flow around the sphere, and the numerical analyses often lack in depicting a thorough investigation of the grid refinement convergence as well as a domain size independence with regards to the calculated drag force. Most articles do not detail the procedure they underwent to obtain an expression for the drag coefficient using numerical and experimental data. Additionally, there were few Carreau fluid studies in the past due to the complexity of the model, although shear thinning fluids will inevitably experience a Newtonian plateau (η_0) in the limit of zero shear rate where the power law model is ill-posed.

This work centers on describing the effect of inelastic shear thinning behaviors on the drag force of a single spherical particle in non-restricted motion. We propose a new stabilized high-order finite element formulation for shear thinning flow, we perform a code verification of the formulation, we present a domain size analysis on the limit cases for the flow-past-a-sphere simulation ranges and a thorough grid convergence analysis, we illustrate the drag coefficients and present a new correlation for the drag coefficient as a function of n and Re for power-law modeled simulations, and we finally discuss Carreau simulation results. Power-law results are compared to numerical results in the literature, and Carreau results are compared to experimental measurements in the creeping flow regime.

The developed framework for shear thinning flows can eventually be extended to more complex geometries, namely for shear thinning flow through packed beds, or for dynamic mixers that treat shear thinning flow.

2. Governing equations and numerical implementation

We consider an incompressible 3D flow inside a domain Ω. In Einstein's notation, the incompressible Navier-Stokes equations are:

$$\partial_l u_l = 0 \tag{1}$$

and

$$\partial_t u_k + u_l \partial_l u_k = -\frac{1}{\rho}\big(\partial_k p + \partial_l \tau_{lk}\big) + f_k \tag{2}$$

where the viscous stress term τ_{lk} is defined by

$$\tau_{lk} = -\eta\big(\partial_l u_k + \partial_k u_l\big) \tag{3}$$

with u_k the k velocity component, ρ the fluid's constant density, p the fluid's pressure, η the fluid's dynamic viscosity and f_k a source term.

For non-Newtonian fluids, η is a function of the shear rate magnitude that needs to be characterized.

2.1. Shear thinning flow

A shear thinning flow is a flow for which the viscosity locally decreases when high shear stresses are applied [3]. At low shear rates, the fluid's viscosity will be constant at η_0 (see region 1 in Fig. 1). This is the initial Newtonian plateau. For very high shear rates, the viscosity of some fluids will reach a second Newtonian plateau at $\eta_\infty \ll \eta_0$ (region 4). A viscosity drop occurs after a critical shear rate (region 3) intrinsic to the fluid. The slope in region 2 characterizes the level of this shear thinning behavior.

The two models used in this work are the power-law model and the four-parameter Carreau model.

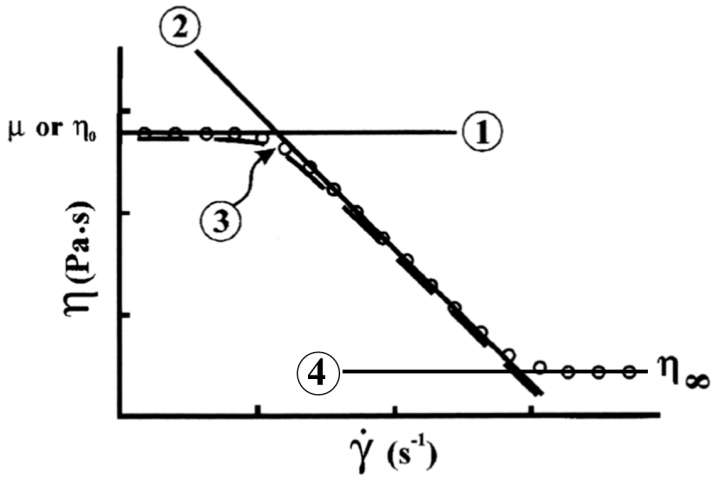

Figure 1: Viscosity regions for shear thinning flows, in log-log scale, with two Newtonian plateaus (1 & 4), a transition (3) to the descending section (2) (adapted from [18]).

2.1.1. Power-law model

This model only requires two parameters and its parameters may easily be found from rheological measurements by linear regression [3]. The viscosity is given by:

$$\eta(\dot{\gamma}) = K\dot{\gamma}^{n-1} \tag{4}$$

where K is the viscosity for a shear rate magnitude of 1.0 s^{-1}, $n-1$ is the slope of $\log(\eta) = f(\log(\dot{\gamma}))$ and $\dot{\gamma}$ is the shear rate magnitude. It adequately captures region 2 (Fig. 1) but fails to represent the η_0 and η_∞ plateaus. It is ill-posed in regions of low to no shear, as the viscosity reaches infinity. This is highly problematic from a computational fluid dynamics (CFD) perspective, since regions of no shear are bound to happen at a point during the solution process.

Since the viscosity is no longer constant, there is an obvious need to redefine the Reynolds number that takes the shear thinning effect around the sphere into

account. As demonstrated in [18], an *a priori* Reynolds number for power-law flow past a sphere is given by:

$$\mathrm{Re} = \frac{\rho |\mathbf{u}|^{2-n} D^n}{K} \tag{5}$$

for which a presumptive apparent shear rate magnitude around the sphere is:

$$\dot{\gamma}_{\mathrm{app}} = \frac{|\mathbf{u}|}{D} [=] \ \mathrm{s}^{-1} \tag{6}$$

with $\mathbf{u} = u_k$.

We note that the given Re in equation (5) represents an *a priori* estimate of the effective Reynolds number. In reality, the shear rate and the viscosity vary abruptly in space. The *a priori* Re is widely used in the literature and helps to compare results.

2.1.2. Carreau model

The four-parameter Carreau model is a generalization of the power-law model that enables to capture both Newtonian regions and the smooth transitions between them and the power-law modeled section. Viscosity as a function of the shear rate is given by:

$$\eta(\dot{\gamma}) = \eta_\infty + (\eta_0 - \eta_\infty)[1 + (\lambda \dot{\gamma})^2]^{\frac{n-1}{2}} \tag{7}$$

where η_0 and η_∞ are respectively the viscosity at rest and the viscosity at high shear rates, λ is the relaxation time, and n is the slope parameter, comparable to that of the power-law model. For the sake of reducing the number of parameters to investigate, and since we know that the shear rates inside Ω will stay in regions 1 and 2 (see Fig. 1), we set $\eta_\infty = 0$. Introducing (6) and (7) into the Reynolds number equation, we get:

$$\mathrm{Re} = \frac{\rho |\mathbf{u}| D}{\eta_0 \left(1 + \left(\lambda \frac{|\mathbf{u}|}{D}\right)^2\right)^{\frac{n-1}{2}}} \tag{8}$$

2.2. Finite element formulation

The non-Newtonian solver is implemented in the open-source CFD software Lethe, based on the `deal.II` framework [19], that uses a Galerkin SUPG/PSPG stabilized finite element formulation approach (see [20] for further details). In this case, the viscosity will vary inside Ω and can no longer be considered a constant. Hence, the finite element weak formulation for steady-state flow becomes:

$$\int_\Omega q\partial_l u_l \mathrm{d}\Omega + \sum_k \int_{\Omega_k} \mathcal{J}_\mathrm{s} \cdot (\tau_\mathrm{PSPG}\partial_l q)\,\mathrm{d}\Omega_k = 0$$
$$\int_\Omega v_k \left(u_l\partial_l u_k - f_k\right)\mathrm{d}\Omega - \int_\Omega \partial_k v_k(p)\mathrm{d}\Omega + \int_\Omega \eta\left(\partial_l v_k\right)\left(\partial_l u_k\right)\mathrm{d}\Omega \tag{9}$$
$$+ \sum_k \int_{\Omega_k} \mathcal{J}_\mathrm{s} \cdot (\tau_\mathrm{SUPG} u_k \partial_l v_k)\,\mathrm{d}\Omega_k = 0$$

with $(v_k, q) \in H_0^1$ the test functions for velocity in the k direction and for pressure, respectively, and $\mathcal{J}_\mathrm{s}$ the strong form of the residual for the momentum equation being:

$$\tau_\mathrm{PSPG} = \tau_\mathrm{SUPG} = \left[\left(\frac{2|\mathbf{u}|}{h_\mathrm{conv}}\right)^2 + 9\left(\frac{4\nu}{h_\mathrm{diff}^2}\right)^2\right]^{-1/2} \tag{10}$$

with $h_\mathrm{conv} = h_\mathrm{diff} = h$ the characteristic size of the cell [21]. The viscosity gradient $\partial_l \eta$ is evaluated using the chain derivative rule:

$$\partial_l \eta = \frac{\partial \eta}{\partial \dot{\gamma}} \partial_l \dot{\gamma} \tag{11}$$

where $\frac{\partial \eta}{\partial \dot{\gamma}}$ is model-dependent, and

$$\partial_l \dot{\gamma} = 2 \cdot \frac{1}{\dot{\gamma}} \cdot \partial_m u_k \left(\partial_l \partial_m u_k + \partial_l \partial_k u_m\right) \tag{12}$$

2.2.1. Implementation challenges

Upon initiation of solving the nonlinear system, the velocity solution vector is often unknown and may be constant (e.g. zero). Thus, the shear throughout the domain is initially zero. Since (12) is undefined for $\dot{\gamma} = 0$, a minimal shear rate magnitude is forced to 10^{-12}, which is small enough to not alter the solution.

A similar problem is encountered when calculating η using equation (4) and when calculating $\frac{\partial \eta}{\partial \dot{\gamma}}$ for power-law fluids. Indeed, neither η nor $\frac{\partial \eta}{\partial \dot{\gamma}}$ are defined for $\dot{\gamma} = 0$ for the power-law model (unlike the Carreau model). Additionally, for low shear rates, since the viscosity is not capped, it can reach excessively high values that are not physical, and that greatly affects the stability of the solver. When using the power-law model, a minimal shear rate $\dot{\gamma}_\mathrm{min}$ is required. This technique is recurrent in commercial CFD software, namely in *Ansys Fluent* [22]. The equivalent maximal viscosity will depend on the chosen K and n parameters (see (4)).

2.3. Drag force

The total drag force felt on a arbitrary object is:

$$F_D = -\left(\int_A \left(\underline{\underline{\sigma}} \cdot \underline{n}\right)\mathrm{d}A\right) \cdot \frac{\mathbf{u}}{||\mathbf{u}||} \tag{13}$$

with A the total surface of the object in contact with the fluid, $\underline{\underline{\sigma}}$ the total stress tensor on the surface, $\underline{n}$ a unit vector normal to the surface of the object, and $\mathbf{u}$ the velocity of the fluid far from the object [23]. The negative sign indicates that we are considering the force of the fluid applied on the particle, in the opposite direction of $\underline{n}$, and the $\frac{\mathbf{u}}{||\mathbf{u}||}$ term allows to only consider the drag component to be in the same direction as $\mathbf{u}$. The total stress tensor has a viscous stress component and a pressure component (14) [3]. The $\underline{\underline{\tau}}$ is significantly affected by the shear thinning behavior on the surface of the object and this changes the resulting viscous drag force (or friction drag force).

$$\underline{\underline{\sigma}} = \underline{\underline{\tau}} + p\underline{\underline{I}} \tag{14}$$

For flow past a spherical object, the drag force is:

$$\boldsymbol{F_D} = \left(\frac{1}{2} A_{\text{eff}} \rho |\mathbf{u}|^2 C_D\right) \frac{\mathbf{u}}{||\mathbf{u}||} \tag{15}$$

where A_{eff} is the effective area of the particle seen from the fluid moving towards it in the $\mathbf{u}$ direction, hence $\pi D^2/4$ for a sphere, and C_D is the drag coefficient [24].

3. Verification of the model using the Method of Manufactured Solutions

We perform a code verification using the Method of Manufactured Solutions (MMS) [25]. This method consists in manufacturing an exact solution for $\mathbf{u}(\mathbf{x}, t)$ and $p(\mathbf{x}, t)$ on a given calculation domain, regardless of its physical plausibility, that is sufficiently complex to ensure a thorough code verification [26]. This means that $\mathbf{u}(\mathbf{x}, t)$ and $p(\mathbf{x}, t)$ should be elements of $\mathcal{C}_{(m+p)}$, where m is larger than the number of times either $\mathbf{u}(\mathbf{x}, t)$ or $p(\mathbf{x}, t)$ is derived in the differential equation and p is the order of the FEM scheme. We then integrate these manufactured solutions in the Navier-Stokes continuity (1) and momentum (2) equations to calculate a source term for the differential equation. We consider the following 2D exact solution in a calculation domain defined by $\Omega = [-1, 1] \times [-1, 1]$:

$$u = \sin(\pi x)^2 \cos(\pi y) \sin(\pi y) \tag{16}$$

$$v = -\cos(\pi x) \sin(\pi x) \sin(\pi y)^2 \tag{17}$$

$$p = \sin(\pi x) + \sin(\pi y) \tag{18}$$

where $\mathbf{u} = [u, v]^T$ and $\mathbf{x} = [x, y]^T$. The velocity and pressure fields are both infinitely differentiable (in $\mathcal{C}_\infty$) because they are built from trigonometric functions. The velocity field is solenoidal, there is therefore no source term in the

continuity equation. Since we consider a steady state problem without any external force, the source term on the momentum equation will take the following form:

$$\mathbf{S} = \begin{bmatrix} u\partial_x u + v\partial_y u + \frac{1}{\rho}\left(\partial_x p + \partial_x \tau_{xx} + \partial_y \tau_{yx}\right) \\ u\partial_x v + v\partial_y v + \frac{1}{\rho}\left(\partial_y p + \partial_x \tau_{yx} + \partial_y \tau_{yy}\right) \end{bmatrix} \tag{19}$$

We use both implemented rheological models for code verification, but we only present the results for Carreau model verification in this article for brevity. Deriving an expression for the shear rate magnitude throughout the domain from (16) and (17), we get that $\dot{\gamma} \in [0, \pi]$. To get an exhaustive verification of the Carreau model by simulating the transition between the initial Newtonian plateau and the descending section of the viscosity (see Fig. 1), we set the following Carreau parameters : $\eta_0 = 1$, $\eta_\infty = 0$, $a = 2$, $\lambda = 1$ and $n = 0.5$, which give us the subsequent expression for viscosity :

$$\eta = (1 + \dot{\gamma}^2)^{-0.25} \tag{20}$$

Hence, the range of viscosity is between 0.551 and 1.000 m^2/s.

Fig. 2 illustrates the $\mathcal{L}^2$ norm of the error for the velocity, as the grid is globally refined, obtained using the stabilized SUPG/PSPG formulation. For Q1 through Q3 elements, the right order of convergence is obtained.

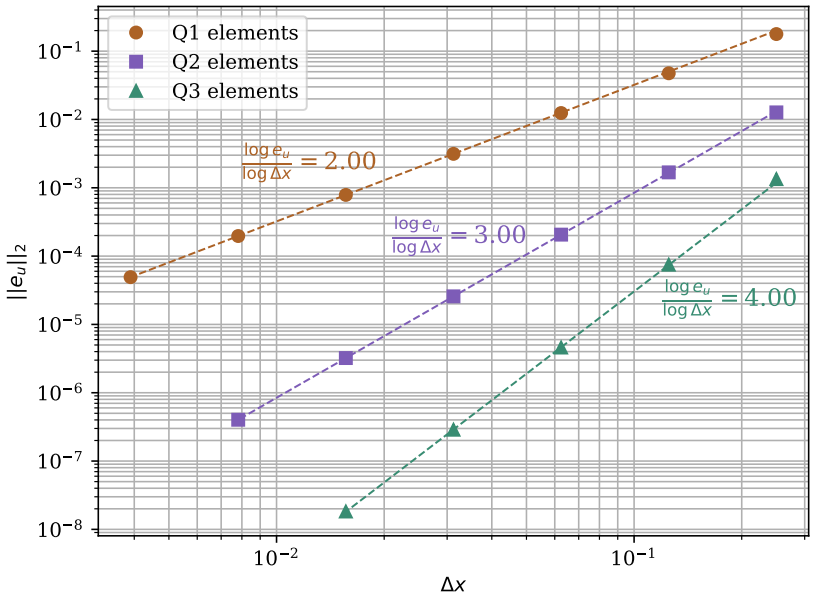

Figure 2: Evolution of the $\mathcal{L}^2$ norm of the error on the velocity profile of a Carreau fluid for different scheme orders when operating a global mesh refinement. The order of convergence is consistent with the order of the underlying FEM interpolation.

4. Non-Newtonian flow past a spherical particle : Results

We present the methodology, including the adopted Re and n ranges and the λ range for simulations using the Carreau model. We discuss the required calculation domain size along with the selected discretization. Subsequently, the results are portrayed and discussed, including a new correlation for the drag coefficients for power-law fluids. We also discuss results using the Carreau model.

4.1. Methodology

The Reynolds number range covered in this work is from 0.1 to 100. A set of 20 Re are used, all log-spaced. For both power-law and Carreau models, a set of eight values of $n \in [0.3, 1.0]$, each linearly-spaced, will be simulated. For Carreau-modeled simulations, for the sake of analyzing dimensionless parameters, dimensionless relaxation times $\Lambda \in [0.1, 0.4, 1, 4, 10, 100]$ will be studied such that:

$$\Lambda = \lambda \dot{\gamma}_{\text{app}} \tag{21}$$

with $\dot{\gamma}_{\text{app}}$ developed in (6).

The geometry for the simulations is given in Fig. 3, where $u_\infty = \mathbf{u}(x) =$ 1 m/s, the particle's diameter D is 1 m, and the height H is determined in section 4.1.1. Thus, for all simulations, $\dot{\gamma}_{\text{app}}$ is 1.0 s^{-1}, and the Reynolds numbers are set by changing K for power-law simulations, and η_0 for Carreau simulations (see equations (5) and (8) respectively). All lateral walls are given a `slip` boundary condition [20].

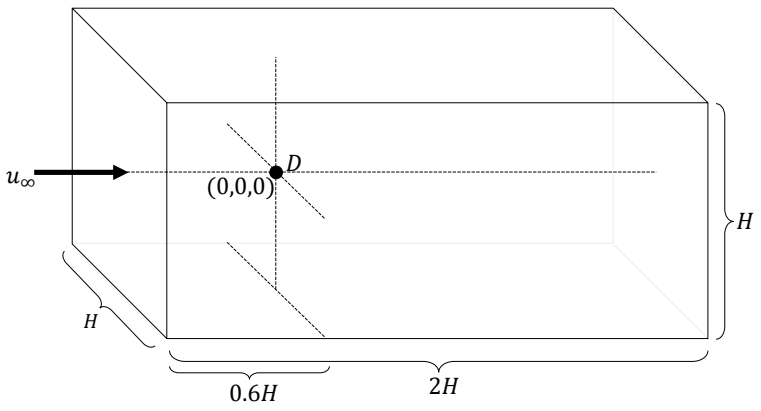

Figure 3: Geometry of the calculation domain and position of the particle for all simulations, with D the diameter of the spherical particle. The dimension H will be determined in section 4.1.1.

We launch all simulations using second-order elements for the velocity interpolation and first-order elements for pressure (Q2Q1). We initially tried Q1Q1

interpolation elements, but these would have required overly fine meshes (and consequently, high number of degree of freedoms) to reach the same level of spatial accuracy. A second order interpolation allows for spatial variation of the shear rate and viscosity within cells. This has a direct impact on the drag force accuracy, and the high-order isoparametric coordinates capture the curvature of the surface of the spherical particles more adequately.

The particle is represented using a high-order sharp-interface immersed boundary method (see [27] for further information on the method). The grid is strategically refined around the particle using a 2-step adaptive refinement technique based on the Kelly error estimator on the velocity [28]. At each refinement step, the convergence criterion on the absolute norm of the solution residual is set to 10^{-5}, and a relative residual of 10^{-7} is obtained with respect to the initial residual. We use a Cartesian 3D grid and choose to simulate on a domain that totally surrounds the particle. If we had chosen to only consider a half or a quarter of the domain cutting through the particle at $(0, 0, 0)$ along the $z-$axis, mesh adaptation would have been hazardous along the axis of symmetry. Moreover, using a domain that encloses the spherical particle greatly helps the iterative solver.

A complete mesh analysis is presented in section 4.1.2. The domain size and mesh-sensitivity analyses are carried out using the power-law model, as power-law fluids simulations are more mesh-sensitive and difficult to simulate.

4.1.1. Domain size

Considering laminar flow past a sphere, at Re = 100, the thickness of the boundary layer is small compared to the sphere diameter [29]. This means that the velocity close to the sphere rapidly reaches u_∞. As the Reynolds number lowers down to 0.1, this boundary layer gradually thickens. The domain size H should be large enough to ensure that the resulting drag coefficient does not vary as the domain is further enlarged for low Re. We carry out the domain size study at Re = 0.1 for Newtonian fluids, as the conclusions can be extended to shear thinning flow (see section 4.2 along with Fig. 11 for validation of this hypothesis). Notice that all studied domains keep the same proportions (see Fig. 3).

Four H/D ratios were analyzed. For each ratio, we use the same $\frac{D}{\Delta x}$ factor close to the surface of the sphere, and we operate a 2-step adaptive mesh refinement targeting 20 % of the cells at each step (further details are given in section 4.1.2). In Fig. 4, we notice that, as the domain becomes larger, the error on the drag coefficient decreases compared to the largest domain. We consider that, for $H/D = 60$, a relative error of less than 0.5% is optimal to simultaneously minimize computational costs and error. The size of the particle is $D = 1$, hence $H = 60$. This domain size will be used for all simulations.

4.1.2. Discretization

Because we are using an immersed boundary method to take the no-slip condition on the surface of the sphere into account, we will not use a conformal grid but rather mesh the entire calculation domain using a structured Cartesian

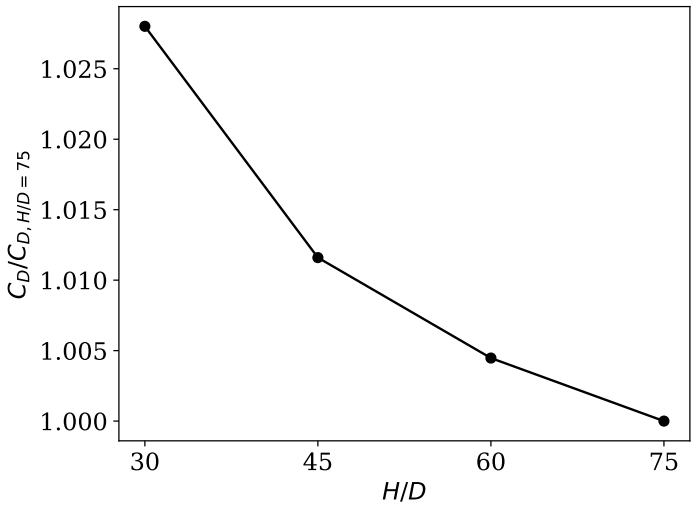

Figure 4: Evolution of the drag coefficient C_D as H/D is increased at Re = 0.1 for Newtonian flow, considering $C_{D,H/D=75} = 244.7$. With an error of less than 1%, the H/D ratio of 60 is chosen.

mesh. This mesh should be fine close to the particle surface to properly capture the flow pattern around it. The mesh should however be coarser farther from the particle, since the flow pattern will not vary as much. We are therefore using a homogeneous grid of $16 \times 8 \times 8$ cells, all of size 7.5^3, that will later be refined around the particle. We then define a refinement zone close to the particle inside which the cells are refined six times. We choose a cubic refinement zone for low Reynolds simulations as the flow is nearly symmetrical on all three axes centering in $(0, 0, 0)$, and we narrow the refinement zone in the $x-$direction for higher Reynolds simulations. For example, at Re = 0.1, the refinement zone is defined by the cube inside $[-2, -2, -2] \times [2, 2, 2]$, and at Re = 100, all cells inside $[-1.5, -1, -1] \times [4, 1, 1]$ are refined six times. The refined cells inside this zone will be of size 0.117^3. For all simulations, this grid is the initial grid, or initial level of refinement, where the smallest cells are of size 0.117^3, and the biggest cells far from the particle are of size 7.5^3. Hence, the initial grids used for the simulations have a characteristic mesh size of $\frac{\Delta x}{D} = 0.117$ around the particle's virtual boundaries (the rightmost points in Fig. 5a and Fig. 5b).

The idea is to keep refining until the simulated drag coefficient does not change any further. At each subsequent refinement step in the simulation (each subsequent points in Fig. 5), we systematically refine each cell inside a hyper-shell zone located inside $0.5\frac{D}{2} \leq \sqrt{x^2 + y^2 + z^2} \leq 1.5\frac{D}{2}$. Simultaneously, we adaptively refine the grid targeting the cells with the greatest error based on the Kelly error estimator applied to the velocity field [28]. Hence, each point in figures Fig. 5a and Fig. 5b within a curve represent a level of refinement in the

same launched simulation. We operate the analysis covering the n range for Re $= 0.1$ and Re $= 100$.

For each simulation, the mesh is refined four times for a total of five levels of refinement, from $\frac{\Delta x}{D} = 0.117$ $\left(\frac{D}{\Delta x} = 8.5\right)$ to $\frac{D}{\Delta x} = 7.3 \times 10^{-3}$ $\left(\frac{\Delta x}{D} = 136\right)$ (the leftmost points in Fig. 5a and Fig. 5b). We can observe in Fig. 5 that for Re $= 0.1$ and for Re $= 100$, the Newtonian solution ($n = 1$) is rapidly mesh-independent. There is a relative error between the calculated drag coefficient for the median refinement at $\frac{\Delta x}{D} = 2.93 \times 10^{-2}$ and the finest mesh of 0.6% for Re $=$ 0.1 and 0.2% for Re $= 100$. We also notice that the solution does not converge as rapidly for shear thinning cases. Indeed, in Fig. 5a, the drag coefficient convergence is delayed as n decreases. For Re $= 100$ (Fig. 5b), reaching a converged solution seems hazardous for shear thinning flow as the evolution of the drag force is not monotonic. This is due to the needed convergence on the viscosity profile, which is not the case for Newtonian simulations. The viscosity range throughout the domain becomes exponentially larger as n decreases; hence the nonlinear component of equation (9) becomes greater and results in a much stiffer problem. For this reason, a thorough mesh-independence study is needed and its importance is even more relevant as n decreases. Conclusions on mesh-independence cannot be drawn from Newtonian simulations only.

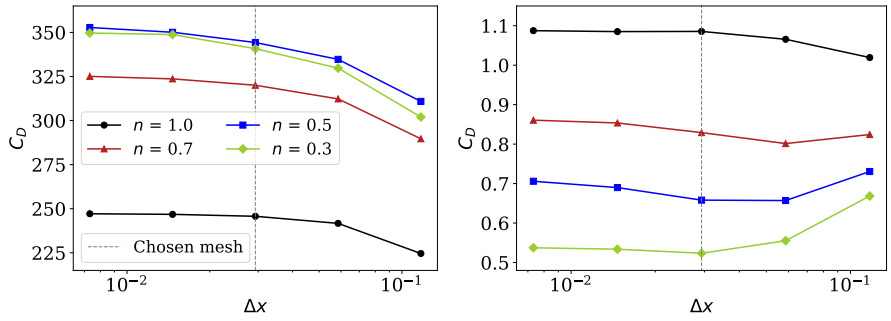

(a) Re $= 0.1$ (b) Re $= 100$

Figure 5: Evolution of the drag coefficient (C_D) as the cells near the particle are refined, for different n values for (a) Re $= 0.1$ and (b) Re $= 100$, using the power-law model. The chosen mesh size ($\frac{\Delta x}{D} = 2.93 \times 10^{-2}$) is in grey.

For all n, the average error calculated between the drag coefficient at $\frac{\Delta x}{D} = 2.93 \times 10^{-2}$ and the most refined mesh ($\frac{\Delta x}{D} = 7.32 \times 10^{-3}$) is below 2%, and the maximal error is encountered at (Re, n) $= (100, 0.5)$ (6.8%). Accessing the next level of refinement ($\frac{\Delta x}{D} = 1.46 \times 10^{-2}$) adds up to 2.4 times the computational costs of reaching the previous level at $\frac{\Delta x}{D} = 2.93 \times 10^{-2}$, and exceptionally 11.1 times for the $(\mathrm{Re}, n) = (100, 0.3)$ case. A level of refinement of $\frac{\Delta x}{D} = 2.93 \times 10^{-2}$ is chosen to minimize the error while maintaining reasonable computational costs.

Fig. 6 presents two examples of meshes used for simulations at Re $= 0.1$ and Re $= 100$. The meshes present eight levels of cell refinement, with the coarsest

cells of size 7.5 and the finest cells of size 2.93×10^{-2}. We notice in Fig. 6a, for Re = 0.1, that cells far from the particle are refined due to velocity diffusion captured by the Kelly error estimator and that the refinement is relatively symmetrical. In Fig. 6b, at Re = 100, with a thin boundary layer and a long wake downstream, the refinement focuses on the particle region and the wake region. We can also acknowledge that all cells inside $0.5\frac{D}{2} \leq \sqrt{x^2+y^2+z^2} \leq 1.5\frac{D}{2}$ have reached the maximal level of refinement.

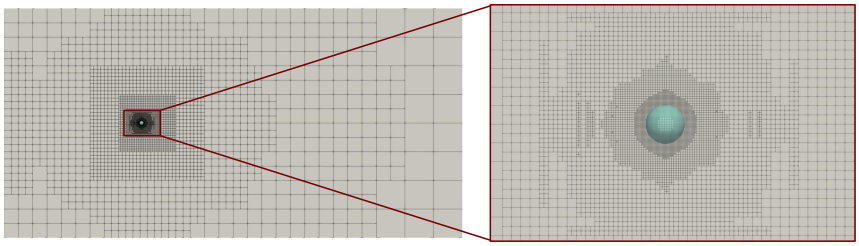

(a) Re = 0.1

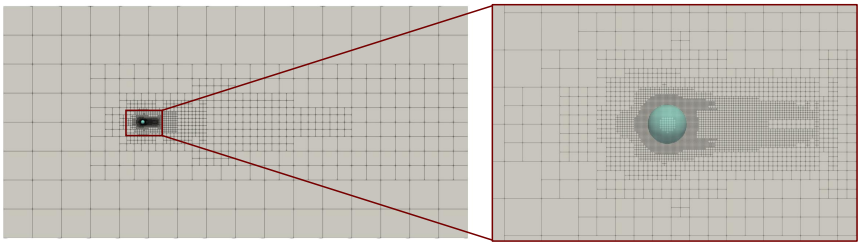

(b) Re = 100

Figure 6: Examples of $xy-$plane mesh slices used for (a) Re = 0.1 and (b) Re = 100, with $H/D = 60$ around the spherical particle (in turquoise).

4.1.3. On choosing a minimal shear rate for power-law simulations

As mentioned in section 2.2.1, the power-law model is ill-posed for problems that encounter very low shear rates, which is the case for this problem. For Re = 0.1, a thorough resolution of the velocity profile further from the particle is important to achieve a drag coefficient convergence. As pictured in Fig. 7, using a $\dot{\gamma}_{\text{min}} = 10^{-2}$ significantly alters the calculated velocity and viscosity profiles, it therefore alters the drag force. For each Re, it is crucial to perform a sensitivity analysis on the minimal shear rate. We choose a value that assures an accurate estimation of the drag force, while again minimizing computational costs and providing converged solutions.

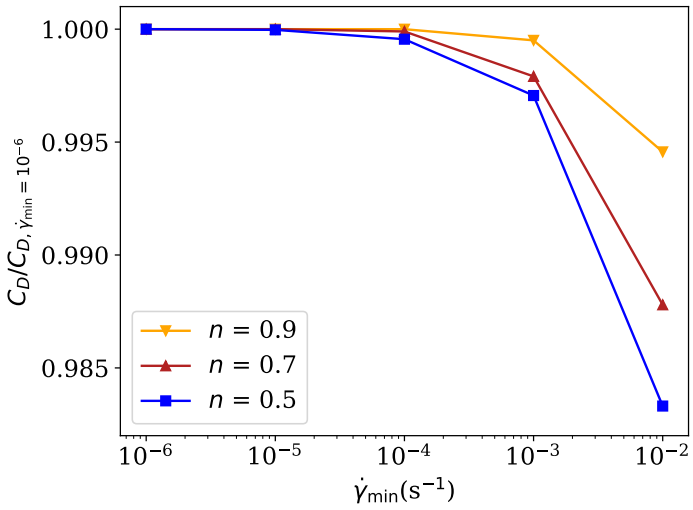

Figure 7: Evolution of the drag coefficient (C_D) for $n = \{0.5, 0.7, 0.9\}$ for a series of minimal shear rate ($\dot{\gamma}_{\text{min}}$) values used for power-law simulations, at Re = 0.1. A $\dot{\gamma}_{\text{min}} < 10^{-4}$ is ideal for Re = 0.1, for all n.

4.2. Results and discussion

We perform all simulations using Lethe. We first run Newtonian flow simulations, and from the vast literature on the single-sphere case, we find the best drag coefficient model to fit our data. We then simulate shear thinning fluids with both power-law and Carreau models.

4.2.1. Model fitting for Newtonian flow

Many models in the literature that cover our simulations Re range (from 0.1 to 100) were compared to our results (see Fig. 8) [30, 31, 32, 33, 11, 34, 35, 36, 37]. Most models are, in general, in excellent agreement with our results (less than 4% error). Dhole *et al.*'s model is a drag correlation developed for shear thinning flows in which we have set n to 1. This model was initially developed to fit a wide range of n, leading to a more significant error (up to 5%) compared to the present work's results than other correlations restricted to Newtonian fluids. On the basis of a least squares method, the model given by Clift *et al.* (see (22)) is easily the most adequate for the range of Reynolds number investigated [38, 30].

$$C_{D,0} = \begin{cases} \frac{24}{\text{Re}}\left[1 + 0.1315\text{Re}^{0.82-0.05\log_{10}\text{Re}}\right], & \text{if Re} \leq 20 \\ \frac{24}{\text{Re}}\left[1 + 0.1935\text{Re}^{0.6305}\right], & \text{if Re} \geq 20 \end{cases} \tag{22}$$

$C_{D,0}$ represents an estimate of $C_D|_{n=1}$ for Re $\in [0.1, 100]$ using Clift *et al.*'s correlation, and $C_{D,0}/C_D|_{n=1}$ is pictured in Fig. 8 in a thick yellow curve. All other models are shown in ascending order of $\mathcal{L}^2$ norm of the error.

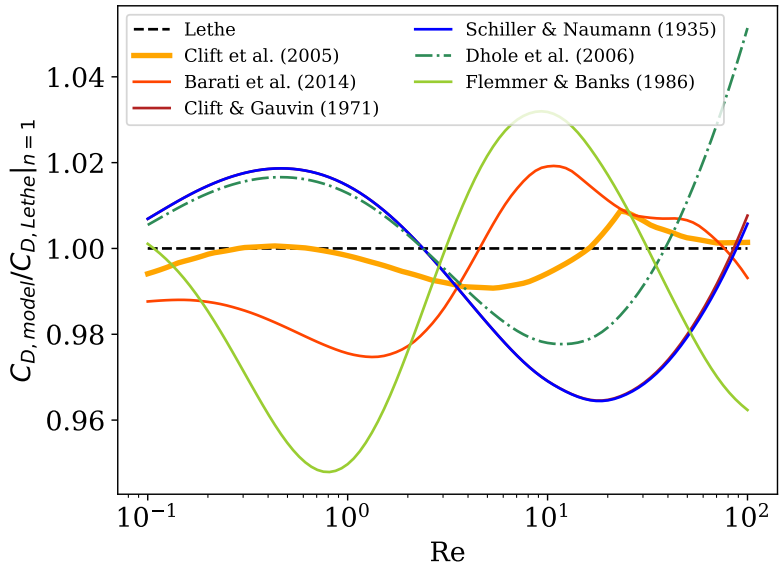

Figure 8: Comparison between drag coefficient models given in the literature and our results for $\mathrm{Re} \in [0.1, 100]$ at $n = 1$ (the ideal ratio is $C_D/C_{D,\mathrm{Lethe}} = 1$, in black) [30, 31, 32, 33, 11, 35]. The chosen model is Clift *et al.*'s, in yellow. The abrupt slope change in the yellow curve at $\mathrm{Re} \approx 23$ is due to the shift in the formulation at $\mathrm{Re} = 20$ (see equation (22)).

4.2.2. Power-law simulation results

We first carry out power-law-modeled simulations for $n \in [0.3, 0.9]$. The drag coefficients for all n values through the Re range are compared to $C_{D,0}$ (22), in order to quantify the effect of shear thinning behaviors on the drag. As many researchers observed, we notice in Fig. 9 that there is a switch in the shear thinning effect close to a Re of 5 or 6 [9, 39, 10, 11]. This phenomena is essentially due to the cessation of the viscosity dominated regime. It looks as though the switch is not at a constant Re for all n. On the right part ($\mathrm{Re} \gtrapprox 5$), we notice that when decreasing n, the drag is commensurately lower than for Newtonian fluids as Re increases. The change of slope for $n \geq 0.6$ at $\mathrm{Re} \approx 23$ is due to the adjustment of the model for $C_{D,0}$ at $\mathrm{Re} = 20$ (see (22)). On the left part ($\mathrm{Re} \lessapprox 5$), as n decreases, the drag seems to be larger as Re decreases up until $n = 0.4$, after which the shear thinning effect decreases. On both sides, the slopes are monotonic for the given Re extent, although they do not seem to diverge : the $C_D/C_{D,0}$ values tend to plateau. We design a correlation that reproduces this pattern.

The chosen form for $C_D/C_{D,0}$ (23) is a hyperbolic tangent centering in $\mathrm{Re_i}(n)$, where $\alpha(n)$ is the amplitude, $\beta(n)$ defines the speed at which $C_D/C_{D,0}$ reaches $\alpha(n)$ on both sides of $\mathrm{Re_i}$ and the vertical displacement is set to 1. All three expressions are shown in equation (24). $\alpha(n)$ is a quadratic function due

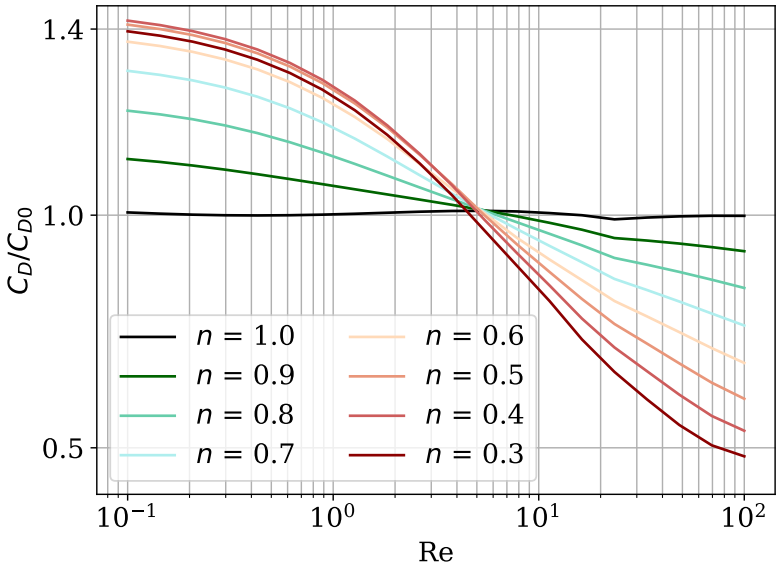

Figure 9: Simulation drag coefficient ratios ($C_D/C_{D,0}$), with $C_{D,0}$ defined in (22), for Re from 0.1 to 100 for all simulated n values using the power-law model. The subtle slope change at Re $\approx$ 23 is due to the formulation change in (22).

to the nonlinearity of $C_D/C_{D,0}|_{\mathrm{Re}=0.1}$. On that matter, other researchers also observed a quadratic pattern in the correction factor for the drag coefficient for creeping flow; indeed, it is found that $C_D/C_{D,0}$ decreases for $n < 0.4$, as seen at the leftmost of Fig. 9 [16, 40]. $\beta(n)$ seems to increase as $1-n$ increases, and $\mathrm{Re_i}$ seems to linearly decrease as $1-n$ increases. The $\mathcal{L}^2$ norm of the error on $C_D/C_{D,0}$ is minimized when splitting the Re extent in two, as the curve pattern is slightly different on both sides. We choose a Re of 6 to split the domain.

$$\frac{C_D}{C_{D,0}}(n,\mathrm{Re}) = \alpha(n)\tanh\left(\beta(n)\log_{10}\left(\frac{\mathrm{Re}}{\mathrm{Re_i}(n)}\right)\right)+1 \tag{23}$$

$$\begin{aligned}\alpha(n) &= \alpha_1(1-n)^2+\alpha_2(1-n)\\ \beta(n) &= \beta_1(1-n)+\beta_2\\ \mathrm{Re_i}(n) &= \mathrm{Re_{i,1}}(1-n)+\mathrm{Re_{i,2}}\end{aligned} \tag{24}$$

Values in Tab. 1 minimize the $\mathcal{L}^2$ norm of the error for $n \in [0.3, 0.9]$ while keeping a maximal error of 0.7% at the junction of each equation for Re = 6.

Fig. 10 portrays the numerical results of the drag coefficients along with the correlation given in equation (23). The average coefficient of determination for the suggested correlation on all n is $R^2 = 0.998$. The drag coefficients are

Table 1: Values for correlation equation (24).

Parameter	$\mathrm{Re} \leq 6$	$\mathrm{Re} \geq 6$
α_1	1.56444	0.50762
α_2	-1.67640	-1.34469
β_1	0.97094	0.25949
β_2	0.45533	0.57677
$\mathrm{Re}_{\mathrm{i},1}$	-3.14987	
$\mathrm{Re}_{\mathrm{i},2}$	6.93023	

compared to other numerical results in the literature [9, 11, 12, 13, 41]. We observe a very satisfying agreement with the previous article's results.

Fig. 11a, 11b and 11c show flow patterns and streamlines close to the particle for Newtonian flow at $\mathrm{Re} = 0.1$, 5.5 and 100, respectively. The subsequent figures show shear thinning flow patterns for n values of 0.7, 0.5 and 0.3.

We notice that, at $\mathrm{Re} = 0.1$, there is no notable difference in the streamlines patterns between n values, but the velocity profile is narrower for lower n, meaning that the velocity around the particle will reach u_∞ more rapidly for lower n. For shear thinning flow, since there is a decrease in viscosity in high shear regions, namely close to the particle in this case, we observe a thinning of the boundary layer. The hypothesis made in section 4.1.1 in which we stated that the domain size analysis could be conducted for $n = 1$ and extended to shear thinning flow is validated, as it seems that the most diffusion of momentum occurs for Newtonian fluids. Although the viscosity is lower close to the spherical particle for lower n values, results show that shear rates observed are greater (see Tab. 2), and that the viscous contribution to the drag does not noticeably change for $\mathrm{Re} \lessapprox 5$. We rather notice that, as n decreases, the upstream-downstream dimensionless pressure difference expands for $\mathrm{Re} = 0.1$ (see Tab. 3), and conclude that the increase of the pressure difference drives the increase on the drag. Indeed, Fig. 12 shows that the pressure drag contribution is proportionally larger as n decreases, and that is the case for the entire Re extent.

Table 2: Dimensionless maximal shear rate on the surface of the sphere for $\mathrm{Re} = \{0.1, 5.5, 100\}$ and $n = \{1, 0.7, 0.5, 0.3\}$ using the power-law model.

	Maximal shear rate		
n	$\mathrm{Re} = 0.1$	$\mathrm{Re} = 5.5$	$\mathrm{Re} = 100$
1	10.6	16.6	49.3
0.7	20.8	24.6	77.5
0.5	36.2	38.5	93.6
0.3	88.2	67.0	106.5

At $\mathrm{Re} = 5.5$, all $C_D/C_{D,0}$ drag coefficient results are similar regardless of n (see Fig. 9), but the velocity profiles are fairly different. It could mean that

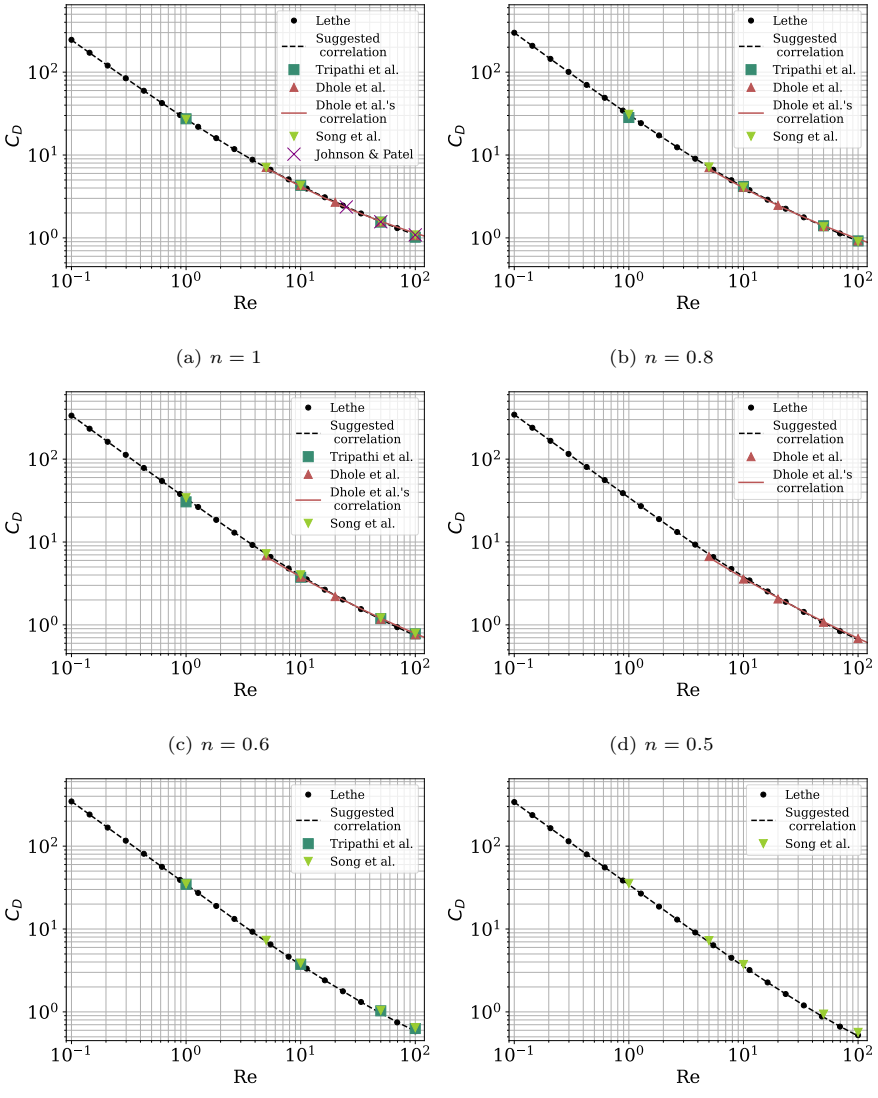

(a) $n = 1$ (b) $n = 0.8$

(c) $n = 0.6$ (d) $n = 0.5$

(e) $n = 0.4$ (f) $n = 0.3$

Figure 10: Calculated drag coefficients for power-law fluids from the Lethe simulations and the suggested correlation compared to results from Tripathi *et al.* [9], Dhole *et al.* [11] and Song *et al.* [12, 13]. Newtonian results ($n = 1$ in (a)) are also compared to Johnson & Patel's [41].

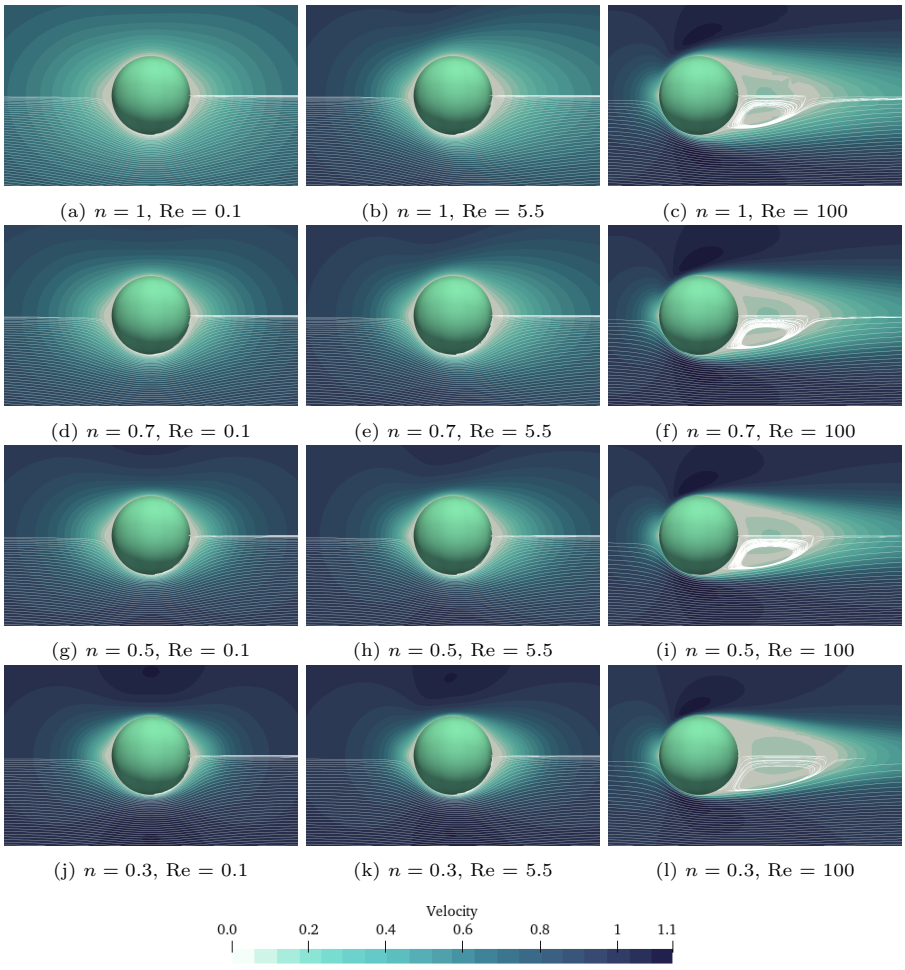

(a) $n = 1$, Re $= 0.1$ (b) $n = 1$, Re $= 5.5$ (c) $n = 1$, Re $= 100$

(d) $n = 0.7$, Re $= 0.1$ (e) $n = 0.7$, Re $= 5.5$ (f) $n = 0.7$, Re $= 100$

(g) $n = 0.5$, Re $= 0.1$ (h) $n = 0.5$, Re $= 5.5$ (i) $n = 0.5$, Re $= 100$

(j) $n = 0.3$, Re $= 0.1$ (k) $n = 0.3$, Re $= 5.5$ (l) $n = 0.3$, Re $= 100$

Figure 11: $xy-$plane velocity profiles with streamlines (in white) around the spherical particle (in turquoise) for Re $= \{0.1, 5.5, 100\}$ and $n = \{1,0.7,0.5,0.3\}$ using the power-law model.

Table 3: Dimensionless upstream-downstream pressure difference on the surface of the sphere for Re = {0.1, 5.5, 100} and n = {1, 0.7, 0.5, 0.3} using the power-law model.

	Upstream-downstream ΔP		
n	Re = 0.1	Re = 5.5	Re = 100
1	6.4e+01	1.9e+00	8.5e−01
0.7	84e+01	2.1e+00	8.5e−01
0.5	1.1e+02	2.3e+00	8.5e−01
0.3	1.2e+02	2.6e+00	8.9e−01

the slight gain in pressure drag (due to the increase of pressure difference (Tab. 3)) is counterbalanced by a drop in viscous drag. From the velocity profiles, no circumstance would explain the switch at Re = 5.5, in addition to the fact that all Reynolds numbers are *a priori* calculated, and hence are not necessarily the effective Re.

At Re = 100, the velocity profile upstream barely changes with n, whereas downstream, the tail seems to be narrower and longer when n lowers (see Tab. 4). As n decreases, the separation point is slightly moved upstream, and the wake is elongated. The enhancement of the tail results in more backflow towards the particle, which reduces the drag. In addition, we notice that the upstream-downstream pressure difference does not vary as n decreases, hence the pressure drag contribution does not vary. This can explain why, at Re $\gtrapprox$ 5, drag forces are lower as n decreases. To summarize, for Re $\lessapprox$ 5, the pressure drag increases as n decreases, and for Re $\gtrapprox$ 5, the viscous drag decreases as n decreases, but the pressure drag does not.

Wake lengths at Re = 100 match those of Dhole *et al.* and Song *et al.*, as can be seen in Tab. 4 [11, 12]. These results, along with comparisons shown in Fig. 10, lend credibility to the developed framework and the results in the present work for the power-law model.

Table 4: Comparison of the dimensionless wake length (L/D) between present work values and values from the literature [11, 12] for power-law fluids.

	Wake length (L/D)		
n	Present work	Dhole *et al.* (2006)	Song *et al.* (2009)
1	0.867	0.88	0.869
0.8	0.872	0.87	0.871
0.6	0.908	0.93	0.898
0.5	0.950	0.96	0.924

4.2.3. Carreau simulation results

As mentioned above, power-law fluids are ill-posed in the zero-shear limit. Carreau fluids have a Newtonian plateau and have a well-defined viscosity at zero shear. For a low dimensionless relaxation time (Λ) fluid, the transition

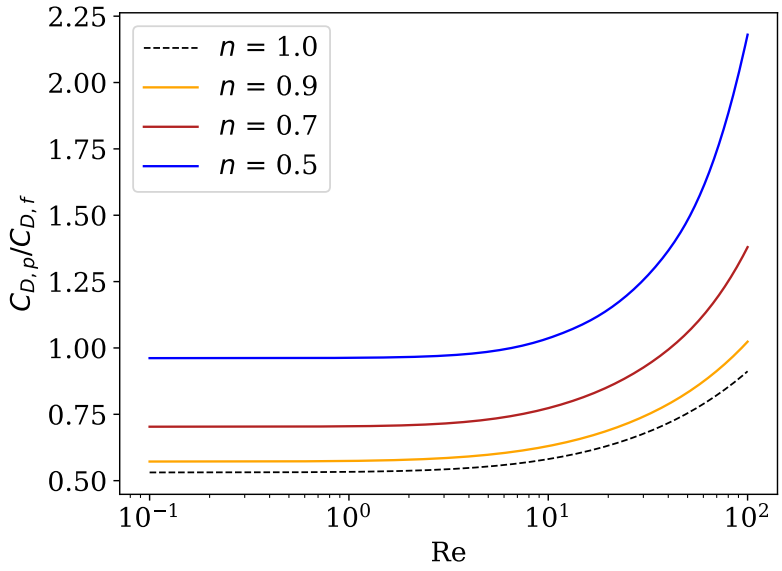

Figure 12: Evolution of the ratio between the pressure drag ($C_{D,p}$) and the friction drag ($C_{D,f}$) for $n = \{1, 0.9, 0.7, 0.5\}$ when increasing the Reynolds number using the power-law model.

from the plateau to the descending region (see Fig. 1) is delayed to high shear rates. Its behavior will resemble the Newtonian behavior. Higher Λ will result in a more power-law-like pattern while never fully reaching it since the shear rate becomes asymptotically zero as the distance from the sphere increases.

Carreau fluids drag coefficient results are shown in Fig. 13 for n values of 0.9, 0.7, 0.5 and 0.3, in which numerous relaxation times are portrayed and compared to power-law and Newtonian results.

For $\Lambda = 0.1$, the drag coefficients are relatively close to those for a Newtonian fluid for all n, as expected. As shown in Tab. 2, the maximal shear rate on the surface of the sphere essentially increases when Re increases. For Re $\lessapprox 5$, the shear rate at the surface of the particle is relatively low, and for $\Lambda \lessapprox 1$, the maximal shear rate is still smaller than the transitioning point in Fig. 1 (region 3). As Re increases, the shear rate close to the particle becomes larger, reaching the critical shear rate, at which point the viscosity decreases. This loss of viscosity, in higher shear rate regions, reduces the drag. Hence, for $\Lambda \lessapprox 1$, a notable difference between the drag given by a Newtonian simulation and a Carreau simulation will only occur at high Reynolds (Re $\gtrapprox 5$). There is therefore no significant change in the drag coefficient for (Re $\lessapprox 5$) up until $\Lambda = 1$.

Considering the given *a priori* Re definition (8), the *a priori* shear rate on the sphere is 1 s^{-1}. This would coincide with the order of magnitude of Λ at which the shear rate on the surface of the sphere is larger than the critical shear

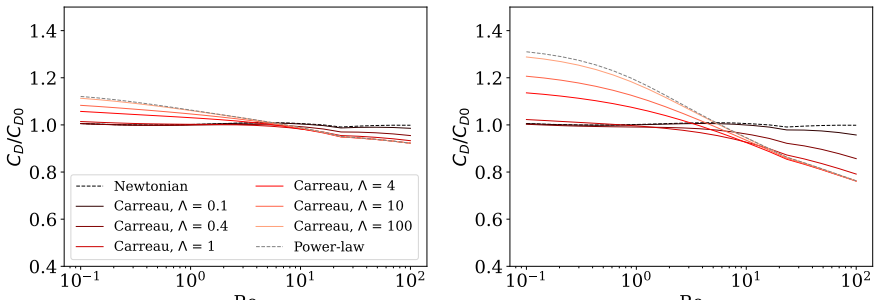

(a) $n = 0.9$ (b) $n = 0.7$

(c) $n = 0.5$ (d) $n = 0.3$

Figure 13: Simulation drag coefficient ratios ($C_D/C_{D,0}$), with $C_{D,0}$ defined in (22) for Re from 0.1 to 100 comparing Newtonian flow, power-law modeled flow and all Carreau modeled simulations for (a) $n = 0.9$, (b) $n = 0.7$, (c) $n = 0.5$ and (d) $n = 0.3$.

rate, even for Re $\lessapprox 5$. For $\Lambda > 1$, as the critical shear rate is lowered (see Fig. 1), the viscosity power-law region takes a more predominant scope, and the drag coefficient is more affected by its shear thinning behavior. We notice that for the highest value of Λ, the drag coefficient profile is very close to that of the power-law curve.

Surprisingly, the calculated drag coefficients for all Carreau fluids do not meet at $C_D/C_{D,0} = 1$ close to Re $= 5.5$ (see Fig. 13). In fact, regardless of n, the drag coefficients for Carreau fluids never exceed either the power-law prediction or the Newtonian prediction. Using a Carreau model does not greatly change the viscosity on the surface of the particle, but at a great distance from the surface, since the viscosity is capped, the flow pattern will inevitably change. When using the power-law model, the drop in viscosity close to the particle reduces the drag, but the very high viscosity far from the particle has an important effect on the drag. With the Carreau model, the upper limit on the viscosity reduces the drag. This may explain why, at Re ≈ 5.5, the Carreau calculated drag coefficients are systematically lower. Indeed, Carreau fluids benefit from a viscosity reduction on the surface of the particle, without having the very high viscosity far from the particle that the power-law model generates.

Flow patterns and streamlines for $n = 0.3$ with $\Lambda = \{0.4, 4\}$ are shown in Fig. 14. In essence, for all pictured Reynolds numbers, the velocity profile has a pattern between the Newtonian flow and the power-law model flow for $n = 0.3$, respectively to their Reynolds number. The $\Lambda = 0.4$ velocity pattern looks closer to the Newtonian one, and the $\Lambda = 4$ resembles the power-law pattern. For Re $= 0.1$ and Re $= 5.5$, we appreciate the forming of a thinner boundary layer for $\Lambda = 4$. For Re $= 100$, a much longer wake region for $\Lambda = 4$ explains the large drop in the drag force observed in Fig. 13d.

As mentioned in the previous section, it is nearly impossible to draw further conclusions comparing the drag coefficients between Λ values at a consistent Re; since all given Re are *a priori* estimations, they are inevitably not effective Re. In fact, many other researchers used a slightly different definition of Re, omitting the n and Λ values [14, 15, 17, 42].

Carreau results at Re $= 0.1$ are compared to experimental drag coefficients presented by Chhabra & Uhlherr in the creeping flow regime [14]. The fluids used in Chhabra & Uhlherr's work are chosen to have the least elastic properties, to best suit the Carreau model that treats inelastic fluids. The article presents results in the fashion of a correction factor to the drag coefficient predicted for Newtonian flow, where $C_{D,0} = 24/\text{Re}$ and the shear-thinning drag coefficient, in creeping flow, being $C_D = XC_{D,0}$. Chhabra & Uhlherr defined their Reynolds as $\text{Re} = \rho u_\infty D/\eta_0$, that is slightly different from equation (8). The present work's Reynolds numbers are adapted to their definition to compare the correction factors appropriately. Since $((1 + \Lambda)^2)^{\frac{n-1}{2}}$ of equation (8) is lesser than 1 for shear thinning flow, the newly calculated Re numbers for Lethe simulations are all less than 0.1. We are, therefore, well into the creeping flow regime. Their dimensionless relaxation times are also corrected, as they used a different definition ($2\lambda u_\infty D^{-1}$). Therefore, their Λ are divided by 2 to match equation

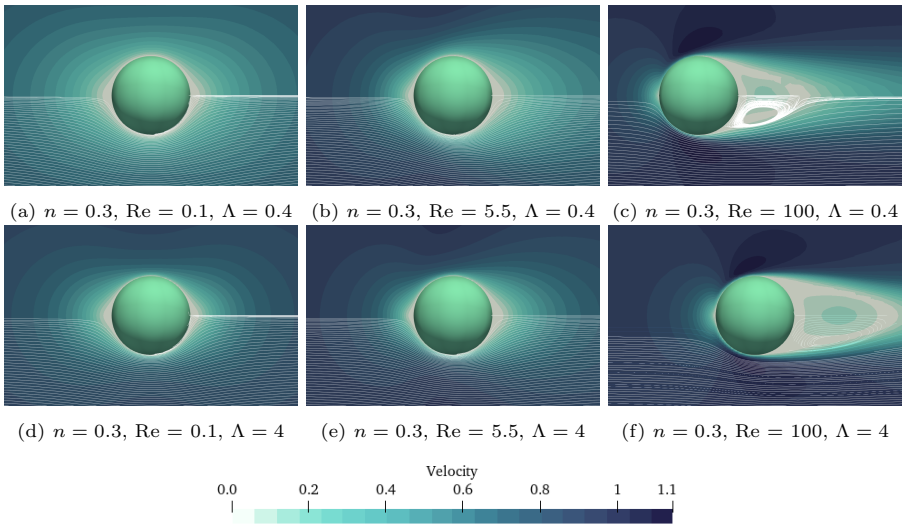

(a) $n = 0.3$, Re $= 0.1$, $\Lambda = 0.4$ (b) $n = 0.3$, Re $= 5.5$, $\Lambda = 0.4$ (c) $n = 0.3$, Re $= 100$, $\Lambda = 0.4$

(d) $n = 0.3$, Re $= 0.1$, $\Lambda = 4$ (e) $n = 0.3$, Re $= 5.5$, $\Lambda = 4$ (f) $n = 0.3$, Re $= 100$, $\Lambda = 4$

Figure 14: $xy-$plane velocity profile with streamlines (in white) around spherical particle (in turquoise) for Re $= \{0.1, 5.5, 100\}$ and $n = 0.3$ using the Carreau model with $\Lambda = \{0.4, 4\}$.

(21).

The correction factors as a function of the dimensionless relaxation time are presented in Fig. 15. As expected, upon decreasing Λ, X reaches 1 as the behavior of the fluid approaches the Newtonian behavior. The drag coefficient decreases as Λ increases; this was also observed by Hsu *et al.* [17]. Experimental results are shown for $n = \{0.75, 0.53\}$, indicating excellent agreement with the numerical results. This validation case lends further credibility to the proposed non-Newtonian framework.

Drag coefficients for Newtonian, power-law and Carreau simulations are available [43].

5. Conclusion

This work presents a stabilized finite element solver extension of Lethe that enables high-order simulations of power-law and Carreau fluids. The implementation is verified using the Method of Manufactured Solutions. We perform an extensive study of shear thinning flow past a sphere. Results for an *a priori* Reynolds range of 0.1 to 100 and $n \in [0.3, 1.0]$ are shown, using both the power-law model and the Carreau model. For the Carreau model, dimensionless relaxation times of $\Lambda \in \{0.1, 0.4, 1, 4, 10, 100\}$ are studied. All calculated drag coefficients are available in a public repository. For shear thinning flow past a sphere a reduction in n has the following effects:

- The total drag increases for Re < 5 to 6;
- The total drag decreases for Re > 5 to 6;

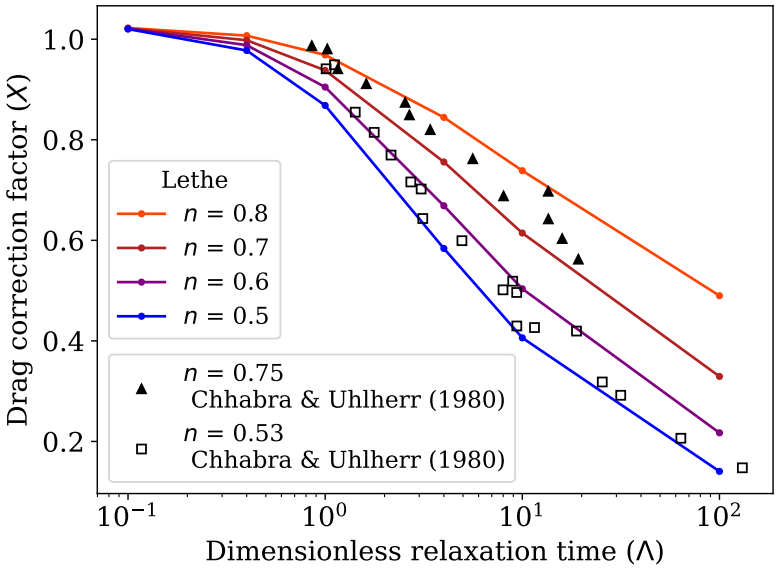

Figure 15: Drag coefficient correction factors (X in $C_D = \frac{24}{\mathrm{Re}}X$) at Re = 0.1 simulated in Lethe using the Carreau model as a function of the dimensionless relaxation time Λ, compared to experimental data provided by Chhabra and Uhlherr [14] in the creeping flow regime.

- The wake is longer for high Re;
- The separation point is moved upstream for high Re; and
- There is the development of a thinner boundary layer, regardless of Re.

Additionally, as Re increases, $C_D/C_{D,0}$ systematically decreases for Re $\in [0.1, 100]$, regardless of the relaxation time. Drag coefficient results using the power-law model are compared to numerical results in the literature and show good agreement. We propose a correlation for the drag coefficient of power-law fluids compared to Newtonian fluids. The correlation is particularly well-posed, we obtain a coefficient of determination $R^2 = 0.998$. It is observed that a logarithmic spacing between the Reynolds numbers used for the simulations greatly helped in generating a formulation that evenly minimized the error over the Re extent, as the behavior of C_D is log(Re)-dependent. The authors believe this correlation can be further extended to lower n values because of the hyperbolic tangent behavior of the correction.

For flow-past-a-sphere cases, using a Carreau model with an appropriate maximal viscosity will significantly impact the velocity profile and the calculated drag force. Considering an *a priori* Reynolds number, power-law and Newtonian simulations predictions will not necessarily bound the drag coefficient of a shear thinning fluid past a sphere. This non-intuitive behavior is explained by the significant decrease of the viscosity far away from the sphere which greatly increases the viscosity of power-law fluids.

6. Acknowledgements

The authors of this article would like to warmly thank the `deall.II` community for their volunteer support. Carole-Anne Daunais is grateful for financial support from the Natural Sciences and Engineering Research Council of Canada (NSERC) through CSG Masters awards, and from the Quebec Research Fund Nature and Technology (QRFNT) through *Bourse de formation à la maîtrise*. Bruno Blais would like to acknowledge the financial support from the Natural Sciences and Engineering Research Council of Canada (NSERC) [RGPIN-2020-04510 Discovery Grant]. The authors would also like to acknowledge technical support and computing time provided by Digital Alliance Canada and Calcul Québec. Simulated cases shown in this work were made on the supercomputers Narval, Niagara and Beluga managed by Digital Alliance Canada and Calcul Québec.

References

[1] H. Brewster, Fluid Mechanics, Oxford Book Company, 2009.

[2] T. Abbasov, S. Herdem, A. Memnedov, On the drag force of a solid sphere in power law flow model, Mathematical and Computational Applications 4 (2) (1999) 161–167. doi:10.3390/mca4020161.

[3] F. Morrison, Understanding Rheology, Raymond F. Boyer Library Collection, Oxford University Press, 2001.

[4] K. Adachi, N. Yoshioka, K. Yamamoto, On non-newtonian flow past a sphere, Chemical Engineering Science 28 (11) (1973) 2033–2043. doi:https://doi.org/10.1016/0009-2509(73)85047-X.

[5] A. Acharya, R. A. Mashelkar, J. Ulbrecht, Flow of inelastic and viscoelastic fluids past a sphere, Rheologica Acta 15 (9) (1976) 454–470. doi:10.1007/bf01530348.

[6] M. A. Lockyer, J. M. Davies, T. E. R. Jones, The Importance of Rheology in the Determination of the Carrying Capacity of Oil-Drilling Fluids, Springer US, Boston, MA, 1980, pp. 127–132. doi:10.1007/978-1-4684-3743-0_27.

[7] G. Dazhi, R. Tanner, The drag on a sphere in a power-law fluid, Journal of Non-Newtonian Fluid Mechanics 17 (1985) 1–12. doi:10.1016/0377-0257(85)80001-X.

[8] Y. Kawase, M. Moo-Young, Approximate solutions for power-law fluid flow past a particle at low reynolds numbers, Journal of Non-Newtonian Fluid Mechanics 21 (2) (1986) 167–177. doi:10.1016/0377-0257(86)80034-9.

[9] A. Tripathi, R. P. Chhabra, T. Sundararajan, Power law fluid flow over spheroidal particles, Industrial & Engineering Chemistry Research 33 (2) (1994) 403–410. doi:10.1021/ie00026a035.

[10] M. Renaud, E. Mauret, R. P. Chhabra, Power-law fluid flow over a sphere: Average shear rate and drag coefficient, The Canadian Journal of Chemical Engineering 82 (5) (2004) 1066–1070. doi:10.1002/cjce.5450820524.

[11] S. D. Dhole, R. P. Chhabra, V. Eswaran, Flow of power-law fluids past a sphere at intermediate reynolds numbers, Industrial & Engineering Chemistry Research 45 (13) (2006) 4773–4781. doi:10.1021/ie0512744.

[12] D. Song, R. K. Gupta, R. P. Chhabra, Wall effects on a sphere falling in quiescent power law fluids in cylindrical tubes, Industrial & Engineering Chemistry Research 48 (12) (2009) 5845–5856. doi:10.1021/ie900176y.

[13] D. Song, R. K. Gupta, R. P. Chhabra, Drag on a sphere in poiseuille flow of shear-thinning power-law fluids, Industrial & Engineering Chemistry Research 50 (23) (2011) 13105–13115. doi:10.1021/ie102120p.

[14] R. P. Chhabra, P. H. T. Uhlherr, Creeping motion of spheres through shear-thinning elastic fluids described by the carreau viscosity equation, Rheologica Acta 19 (2) (1980) 187–195. doi:10.1007/bf01521930.

[15] R. P. Chhabra, P. H. T. Uhlherr, Sphere motion through non-newtonian fluids at high reynolds number, The Canadian Journal of Chemical Engineering 58 (1) (1980) 124–128. doi:10.1002/cjce.5450580120.

[16] M. Bush, N. Phan-Thien, Drag force on a sphere in creeping motion throug a carreau model fluid, Journal of Non-Newtonian Fluid Mechanics 16 (3) (1984) 303–313. doi:https://doi.org/10.1016/0377-0257(84)85016-8.

[17] J. Hsu, S. Yeh, S. Tseng, Drag on a sphere in a spherical dispersion containing carreau fluid, Powder Technology 188 (1) (2008) 34–41. doi:10.1016/j.powtec.2008.03.014.

[18] P. J. Carreau, D. C. R. D. Kee, R. P. Chhabra, Rheology of Polymeric Systems, Hanser Fachbuchverlag, 2021.

[19] D. Arndt, W. Bangerth, M. Feder, M. Fehling, R. Gassmöller, T. Heister, L. Heltai, M. Kronbichler, M. Maier, P. Munch, J.-P. Pelteret, S. Sticko, B. Turcksin, D. Wells, The deal.II library, version 9.4, Journal of Numerical Mathematics 0 (0). doi:10.1515/jnma-2022-0054.

[20] B. Blais, L. Barbeau, V. Bibeau, S. Gauvin, T. E. Geitani, S. Golshan, R. Kamble, G. Mirakhori, J. Chaouki, Lethe: An open-source parallel high-order adaptative cfd solver for incompressible flows, SoftwareX 12 (2020) 100579. doi:https://doi.org/10.1016/j.softx.2020.100579.

[21] T. Tezduyar, S. Sathe, Stabilization Parameters in SUPG and PSPG Formulations, Journal of Computational and Applied Mechanics (4) (2003) 71–88. doi:10.1016/j.cma.2005.05.032.

[22] Viscosity for non-newtonian fluids, https://www.afs.enea.it/project/neptunius/docs/fluent/html/ug/node297.htm, Online; accessed 2 September 2022.

[23] G. K. Batchelor, An Introduction to Fluid Dynamics, Cambridge University Press, 2000.

[24] G. W. Griffiths, Numerical Analysis Using R, Cambridge University Press, 2016.

[25] W. L. Oberkampf, Verification and validation in scientific computing, Cambridge University Press, 2010.

[26] P. J. Roache, Verification and validation in computational science and engineering, Hermosapublishers, 1998.

[27] L. Barbeau, S. Etienne, C. Béguin, B. Blais, Development of a high-order continuous galerkin sharp-interface immersed boundary method and its application to incompressible flow problems, Computers & Fluids 239 (2022) 105415. doi:10.1016/j.compfluid.2022.105415.

[28] D. W. Kelly, J. P. D. S. R. Gago, O. C. Zienkiewicz, I. Babuska, A posteriori error analysis and adaptive processes in the finite element method: Part i—error analysis, International Journal for Numerical Methods in Engineering 19 (11) (1983) 1593–1619. doi:10.1002/nme.1620191103.

[29] H. Schlichting, J. Kestin, Boundary layer theory, Vol. 121, Springer, 1961.

[30] R. Clift, J. R. Grace, M. E. Weber, Bubbles, drops and particles, Dover Publications, Mineola, N.Y., 2005.

[31] R. Barati, S. A. A. S. Neyshabouri, G. Ahmadi, Development of empirical models with high accuracy for estimation of drag coefficient of flow around a smooth sphere: An evolutionary approach, Powder Technology 257 (2014) 11–19. doi:10.1016/j.powtec.2014.02.045.

[32] R. Clift, W. H. Gauvin, Motion of entrained particles in gas streams, The Canadian Journal of Chemical Engineering 49 (4) (1971) 439–448. doi:10.1002/cjce.5450490403.

[33] L. Schiller, Z. Naumann, A drag coefficient corre-lation, VDI Zeitungk 77 (1935) 318–320.

[34] P. P. Brown, D. F. Lawler, Sphere drag and settling velocity revisited, Journal of Environmental Engineering 129 (2003) 222–231. doi:10.1061/(ASCE)0733-9372(2003)129:3(222).

[35] R. Flemmer, C. Banks, On the drag coefficient of a sphere, Powder Technology 48 (3) (1986) 217–221. doi:10.1016/0032-5910(86)80044-4.

[36] H. Brauer, D. Mewes, Strömungswiderstand sowie stationärer und instationärer stoff- und wärmeübergang an kugeln, Chemie Ingenieur Technik 44 (13) (1972) 865–868. doi:10.1002/cite.330441314.

[37] F. F. Abraham, Functional dependence of drag coefficient of a sphere on reynolds number, Physics of Fluids 13 (8) (1970) 2194. doi:10.1063/1.1693218.

[38] J. Wolberg, Data Analysis Using the Method of Least Squares, Springer, 2006.

[39] D. Graham, T. Jones, Settling and transport of spherical particles in power-law fluids at finite reynolds number, Journal of Non-Newtonian Fluid Mechanics 54 (1994) 465–488. doi:10.1016/0377-0257(94)80037-5.

[40] I. Machač, B. Šiška, Calculation of terminal falling velocity of sphericalparticles moving through polymer solutions usinga power-law viscosity model, Scientific papers of the University of Pardubice (25) (2019) 117–126.

[41] T. A. Johnson, V. C. Patel, Flow past a sphere up to a reynolds number of 300, Journal of Fluid Mechanics 378 (1999) 19–70. doi:10.1017/s0022112098003206.

[42] R. P. C. Doayun Song, Rakesh K., Wall effect on a spherical particle settling along the axis ofcylindrical tubes filled with carreau model fluids, 2011.

[43] [dataset], C.-A. Daunais, Shear thinning flow past a sphere drag coefficients results (Power-law and Carreau), https://github.com/lethe-cfd/lethe-utils/tree/master/cases/non_newtonian/sphere (2022).